Generation of synchronized high-frequency triaxial magnetic fields using fractal capacitor banks

Javier Tajuelo[,†] Óscar Martínez-Cano, Jose R. Morillas[,‡] Jianjian Yang[,§] and Juan de Vicente[*]
F2N2Lab, Magnetic Soft Matter Group and Excellence Research Unit 'Modeling Nature' (MNat), Department of Applied Physics, Faculty of Sciences, University of Granada, C/Fuentenueva s/n, Granada 18071, Spain

Magnetic field generators with the ability to create well-controlled dynamic fields in arbitrary directions are an essential tool to investigate magnetic soft matter and to drive (sub)micrometer structures to targeted locations. In this article we present the design and performance of a triaxial generator based on three fractal capacitor banks that enable real-time control of the output field and a quasi-continuous distribution of resonant frequencies up to 4 kHz. The increased field strength over the entire frequency range will enhance the response of magnetorheological fluids as well as the velocity and load capacity of magnetic swarms that, in recent years, have made the leap from *in vitro* to *in vivo* studies of targeted drug delivery.

I. INTRODUCTION

Well-controlled dynamic magnetic fields have been successfully used for the wireless transfer of energy to micropropellers. Inspired by the strategies that microorganisms have evolved to swim, numerous artificial microrobotic systems have been developed, making this field promising in a biological or biomedical context. Artificial flexible flagellum [1], helical swimmers [2], and adaptive microswarms based on collective behavior [3,4] have been reported. Interestingly, upstream motion has also been achieved [5–7] mimicking rheotaxis strategies of natural microswimmers such as spermatozoa [8,9], bacteria [10,11], and plankton [12], where the no-slip boundary condition in a wall is utilized to swim against the flow. In addition, the natural evolution of the research on artificial micropropellers from *in vitro* to *in vivo* applications already started in the last decade [13,14], where, for instance, magnetotactic bacteria were used as carriers of drug-loaded nanoliposomes into hypoxic regions of a tumor in a mouse [15,16].

From a different research perspective, a particularly interesting family of colloidal systems is that of magnetic colloids [17] and more precisely magnetorheological (MR) fluids [18,19]. Typically, these are suspensions of magnetic-field-responsive micrometer-sized particles that experience a liquid-to-solid transition under a magnetic field. These intelligent materials have already reached the market in a number of applications involving linear and angular momentum transfer (e.g., brakes, shock absorbers, or artificial joints [20]). Traditionally, field configurations employed in MR fluids are uniaxial dc or pulselike [21–24]. However, aggregation and propulsion studies reporting structural and/or dynamical properties also exist under rotating fields [23,25,26], uniaxial dc + oscillating fields [27,28] and uniaxial dc + rotating fields [29]. In all cases, experiments are limited to low excitation frequencies (below about 10 Hz). More recently, it has been shown that triaxial fields are particularly suitable to generate a strong fluid vorticity [30,31], which is a relevant phenomenon to problems involving heat and mass transfer.

In this article we present the details and analyze the performance of a triaxial magnetic field generator with dynamic control capability, so that an arbitrary time-dependent magnetic field $\mathbf{H}(t)$ can be generated in a volume or region of interest (ROI). The instrument is designed to optimize its performance in a wide range of frequencies, so that high-intensity fields can be generated from dc to several kilohertz in a quasi-continuous manner. Through experiments and finite-element method (FEM) simulations, we have characterized and tested the device in different configurations, showing that it

---

*Corresponding author. jvicente@ugr.es
†Current Address: Department of Interdisciplinary Physics, Universidad Nacional de Educacion a Distancia UNED, Avda. Esparta s/n, 28232 Las Rozas, Spain.
‡Current Address: Benjamin Levich Institute, City College of New York, 10031 New York, USA.
§Current Address: Department of Chemistry and Material Engineering, Logistic Engineering University, Chongqing 401311, People's Republic of China.

can overcome the intensity-to-frequency ratio limitations in biomimetic artificial micropropellers and MR fluids research.

II. DESIGN OF THE TRIAXIAL GENERATOR

The triaxial generator was conceived following three main goals: (i) enhance the field homogeneity in the ROI; (ii) allow for the generation of alternating fields in a broad range of frequencies with a single instrument (no need for any hardware manipulation); and (iii) generate arbitrary dynamic magnetic fields. These three characteristics have been achieved, respectively, by means of an optimal instrument's geometry through FEM simulations, three fractal capacitor banks controlled by a customized feedback loop, and a dedicated LabVIEW software to generate arbitrary voltage signals that takes into account the known impedance of each circuit.

The schematics of the triaxial generator is shown in Fig. 1. It consists of five coil+yoke subsystems, where each one of them can be independently fed. The yokes allow us to reach high fields. They are made of MuMETAL (Magnetic Shield Corp.) so that high-frequency fields can be created without great losses. Four coil+yoke subsystems are identical and are fixed in space, with their axes in the horizontal plane. Two of them have their axes along the X direction and are facing each other at a distance of $2d_y$, whereas the other two are placed in a similar fashion along the Y direction.

The fifth coil+yoke subsystem is placed at the bottom of the generator, having its axis vertically aligned along the Z axis. In order to perform MR experiments by placing the generator under a torsional rheometer, only one coil is used in the Z axis to have access to the ROI. Four micrometer heads allow for the vertical displacement of the fifth coil+yoke subsystem in such a way that the upper base of the vertical yoke spans from $z = -28.8$ mm to $z = 1.3$ mm. In all the verification experiments reported in this work, the ROI sits on top of a plastic holder with a height of 17 mm which, in turn, is attached on top of the vertical yoke (thus, in all experiments the upper base of the vertical yoke is at $z = -17$ mm). Both the micrometer heads and the holder allow us to finely align the ROI with the plane that contains the horizontal coil+yoke subsystems. Further technical details about the amplifiers, DAQ board and relays used to build the generator are provided in the Supplemental Material [32].

A. Fractal capacitor banks

Working at the resonance of a R–L–C circuit is the most direct way to maximize the magnetic field generated by a coil-based setup, but a set of capacitors controlled by a selector switch or a parallel/disconnected capacitor bank [33,34] cannot provide a quasi-continuous distribution of
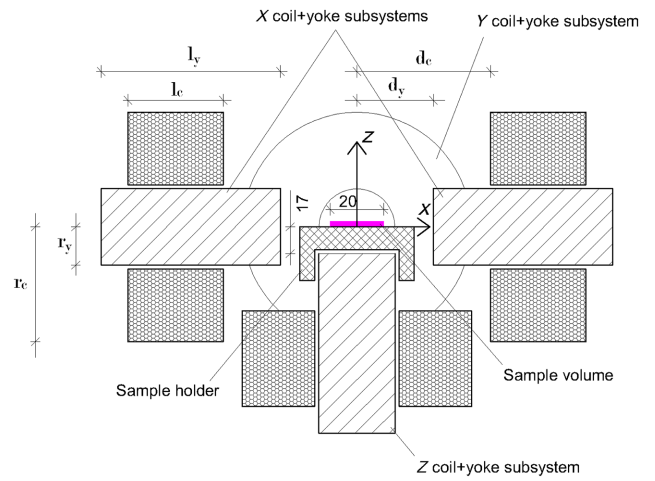

FIG. 1. Schematics of the triaxial generator along with the used frame of reference. The Z coil+yoke subsystem can be vertically displaced. In this article, the position of the upper base of the vertical yoke is $z = -17$ mm, so that the surface of the ROI is conveniently located at $z = 0$. Note that the subscript "y" denotes "yoke".

capacitance values with a reasonable number of capacitors. Therefore, inspired by the design proposed by Martin [35], we built three synchronized fractal capacitor banks connected to the three circuits that control the components of **H** along the three directions of space. The three circuits work independently but are controlled by the same dedicated software developed in LabVIEW.

Each capacitor bank comprises N different capacitors, where the connection of each capacitor to the circuit is controlled by two relays as indicated in Fig. 2. Starting from the left-hand side, the first capacitor can be shunted (switch $S_{1A} = $ CLOSE, switch $S_{1B} = $ OPEN) or connected (switch $S_{1A} = $ OPEN, switch $S_{1B} = $ CLOSE). The rest of the capacitors can be shunted ($S_{nA} = 1$, $S_{nB} = $ OPEN), in series with those capacitors placed on their left ($S_{nA} = 2$, $S_{nB} = $ OPEN), or in parallel with those capacitors placed on their left ($S_{nA} = 1$, $S_{nB} = $ CLOSE). For a bank with N capacitors, there are $2 \times 3^{N-1}$ different connection modes (states), from which we have to eliminate: (i) 2^{N-1} states that are equivalent to a short-circuit and (ii) $S(N, 3)$ states whose equivalent capacitance is given by other state. Here $S(N, 3)$ represents the Nth Stirling number of the second kind. Therefore, the number of different states is $2 \times 3^{N-1} - 2^{N-1} - S(N, 3)$, each one defined by N coordinates indicating the type of connection of the capacitors (in series, in parallel, or shunted). The value of the equivalent capacitance for each state, $C_{eq}^{\{n\}}$, is within the interval $[C_{eq}^{\{min\}}, C_{eq}^{\{max\}}]$, where $C_{eq}^{\{min\}}$ corresponds to the all-in-series state and $C_{eq}^{\{max\}}$ to the all-in-parallel state.

Given the inductance, L, of each pair of coils in the XY plane (~ 40 mH), the circuits can work without a significant loss in the I/V ratio up to ~ 40 Hz. Moreover,
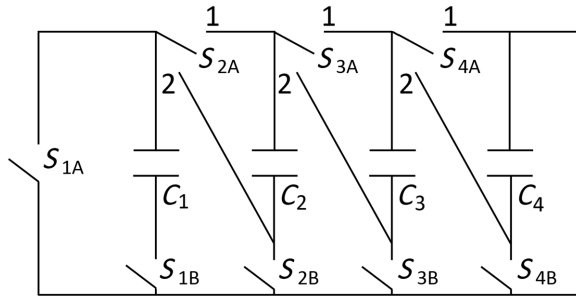
FIG. 2. Schematics of the fractal capacitor bank, where C_1 can be shunted or connected, and the rest of capacitors can be shunted, in series, or in parallel with those capacitors on their left.
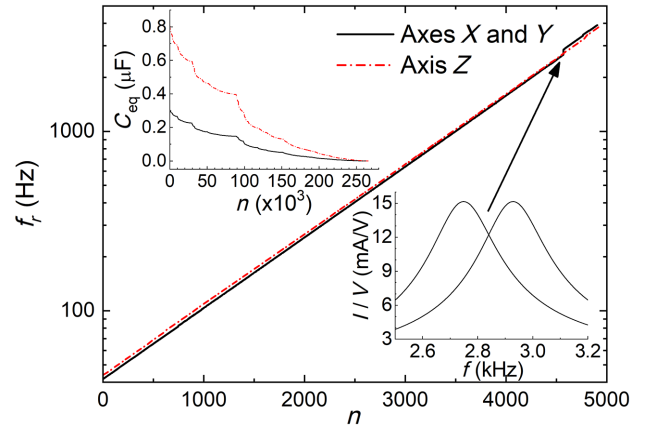

FIG. 3. Results of the calibration using states with resonant frequencies separated by a $\sim 0.1\%$. The top left inset plot represents the nominal equivalent capacitance of all the possible states of the capacitor bank. The bottom right inset plot represents the I/V ratio versus frequency corresponding to those states showing the largest increment. Note that this increment can be seen as a small step in the solid curve.

the self-induced eddy current losses make the apparent resistance of the circuit increase at large frequencies, limiting the performance of the coil + capacitor bank system at a maximum of ~ 4 kHz (see Supplemental Material for measurements on the I/V ratio versus frequency [32]). Therefore, we selected a set of capacitors such that the minimum and maximum resonant frequencies (corresponding to $C_{\mathrm{eq}}^{\{\max\}}$ and $C_{\mathrm{eq}}^{\{\min\}}$, respectively) are as close as possible to 40 and 4000 Hz. The nominal values of the capacitors comprising each bank were chosen to make the distribution of the resonant frequencies as continuous as possible. Referring to the nominal capacitance of each capacitor as C_i, with $i \in [1, N]$, the optimal distribution of resonant frequencies is achieved for a set of capacitors satisfying $C_i = 2C_{i-1}$ [35]. Considering the number of different states as a function of N, 12 capacitors for each bank were used, obtaining 265 720 different states. The set of 12 capacitance values was chosen from those commercially available to satisfy, as closely as possible, the following relations:

$$f_r^{\min} = \frac{1}{2\pi \sqrt{L \sum_{i=1}^{N} C_i}} \simeq 40 \text{ Hz},$$

$$f_r^{\max} = \frac{1}{2\pi \sqrt{L \left(\sum_{i=1}^{N} \frac{1}{C_i} \right)^{-1}}} \simeq 4000 \text{ Hz}, \quad (1)$$

$$C_i = 2C_{i-1}.$$

The nominal capacitance and manufacturer of all the capacitors selected for each circuit are indicated in the Supplemental Material [32]. Considering those nominal values and the bank architecture, we calculated the equivalent capacity for all the possible states, $C_{\mathrm{eq}}^{\{n\}}$, which we represent in the top left inset of Fig. 3, where the different states, n, have been sorted in decreasing $C_{\mathrm{eq}}^{\{n\}}$ values. As can be seen, the dependence of $C_{\mathrm{eq}}^{\{n\}}$ on n is not linear, i.e., the values of $C_{\mathrm{eq}}^{\{n\}}$ are not equally distributed and many of them are indistinguishable in practice. In the spirit of Ref. [35], we

have selected a subset of states where the gaps in nominal resonant frequency between consecutive states is as close as possible to 0.1%, obtaining 4905 states for the X and Y circuits, and 4934 states for the Z circuit [35].

B. FEM simulations

The optimal geometry of the generator was obtained after performing a series of FEM simulations using COMSOL Multiphysics. In these simulations, the size and position of the coil+yoke subsystems were systematically changed looking for a compromise between field magnitude (evaluated through the volume average of the magnetic field magnitude) and homogeneity (evaluated through its standard deviation in the ROI; a vertically aligned cylinder 10 mm in radius and 100 µm in height). When optimizing the geometry, it was taken into account that the full generator geometry should not be wider than 175 mm and that any of its pieces must not be closer than 15 mm to the center (except for the Z subsystem), so that it fits in a regular torsional rheometer for MR fluid characterization. In addition, the simulations were also used to validate the experimental characterization of the device. The comparison between the optimal geometry provided by the FEM simulations and the actual size of the device is listed in the Table I, where deviations of the actual values with respect to the optimal ones are within 4%.

Details on the method, computational box, and mesh size of the numerical scheme are depicted in the Supplemental Material, along with a summary of the optimization results [32]. The simulations demonstrate that smaller distances between the center of the device and the yokes do not improve the homogeneity as numerical results point

TABLE I. Optimum and actual values of the different geometrical parameters of the triaxial generator. The description of all these parameters is depicted in the schematics of the device, Fig. 1. Note that the subscript "y" denotes "yoke".

Parameter	X and Y Optimum (mm)	Actual (mm)	Z Optimum (mm)	Actual (mm)
l_y	68	68	*	68
r_y	*	12.5	*	12.5
d_y	17	17.5	17	17
l_c	30	30	36	36
r_c	37	36	*	30
d_c	40	39	34	33

*These parameters are not optimized but fixed at the actual values.

that yokes should be further separated to reduce inhomogeneity. However, they create a larger field strength where the inhomogeneity is within an acceptable working range for our intended applications.

C. Ensuring synchronization between independent circuits

A precise control of the strength and direction of **H** is required for any application, where both parameters must be dynamically tunable. Thus, the intensity and relative phase of the three circuits must be well synchronized. In contrast to what one might initially suspect, such synchronization in R–L–C circuits where the capacitance is adjustable as explained previously, is far from trivial and is not feasible through a simple synchronization of the voltage output of the amplifiers that feed the circuits. As we show in the Supplemental Material [32], a small deviation of $\pm 5\%$ from the nominal value of the capacitance (which may take place due to temperature effects) yields to phase lag errors as large as $50°$ for a resonant frequency of only 180 Hz. Under those circumstances, a targeted rotating field (circular) would yield to a nonconstant strength field (elliptical). To ensure that the actual field exactly follows the prescribed one, we have developed a feedback control loop that fine-tunes the amplitude and phase of the signals driving the amplifiers. Since the working conditions of the circuits may change (especially due to temperature effects), the feedback control loop must be running on the fly over the whole duration of the experiment. For this reason, we chose to develop a single LabVIEW code that controls all the elements of the system: it selects the most suitable state for the frequency input by the user and continuously fine-tunes the signal driving the amplifiers to match the target currents and phase lags. Further details on the flowchart of the feedback control loop are given in the Supplemental Material [32].

III. RESULTS

A. Characterization of the triaxial generator

We have calibrated each capacitor bank using a dedicated LabVIEW code that, for each state, performs a frequency sweep and finds the actual values of the equivalent capacitance and the resonant frequency, $C_{eq}^{\{n\}}$ and $f_r^{\{n\}}$. Details on this calibration procedure are depicted in the Supplemental Material [32]. The results of the calibration are shown in Fig. 3, where the actual resonant frequencies for the 4905 states are plotted. To evaluate the quasi-continuous response of the capacitor bank, the actual gap between consecutive states was calculated, finding that most of them are well below 1% whereas the largest gap is $\sim 6.5\%$ (between states $n = 4568$ and $n = 4569$ of the X and Y circuits). This gap is indicated with the arrow in Fig. 3, where a small step can be seen in the solid curve. The bottom right inset plot represents the current to voltage ratio, I/V, for the states $n = 4568$ and $n = 4569$, where their overlapping allows us to safely assume that the distribution of resonant frequencies is continuous in practice.

During the experiments, the measured quantity is the electrical current in the circuits, while the target quantity is **H**. The ratio between both quantities, that we refer to as K, has been characterized for the three circuits. The magnetic field strength created in the center of the device by a dc current is represented in Fig. 4(a). As expected, the dependence on the intensity current is fairly linear, where the fit to the data yields $K_x = K_y = 7.77$ (kA/m)/A and $K_z = 2.80$ (kA/m)/A. Numerical results according to FEM simulations are shown with stars, where an excellent agreement with the experimental results is observed. Figure 4(b) represents the dependence of K_x, K_y, and K_z on the frequency. Although a small decrease on H was observed for the X and Y axes (probably due to the limitations of the teslameter at high frequencies), K_x, K_y, and K_z are assumed to be constant and the values obtained for the dc case are used without any correction for the ac experiments.

The homogeneity of **H** is another important parameter because the ROI is typically large compared with the size of the micropropellers or particle aggregates. In the following analysis we will assume that the coordinates origin is located at the center of the device and the ROI is placed at the origin. Figure 5(a) shows H_x and H_z along the X axis and Fig. 5(b) shows H_z along the Z axis. In all cases, a current of 1 A was used. The shaded regions in Figs. 5(a) and 5(b) represent the ROI. As observed, the field strength at the edge is about $\sim 18\%$ larger than the value at the center, whereas there is no significant differences between the bottom and the top boundaries. More importantly, the gradients $\partial H_x / \partial x$ and $\partial H_z / \partial x$ equal zero only at $x = 0$. In other words, magnetophoretic forces can only be neglected at the center. Regarding FEM results, small differences can be seen with experiments, probably
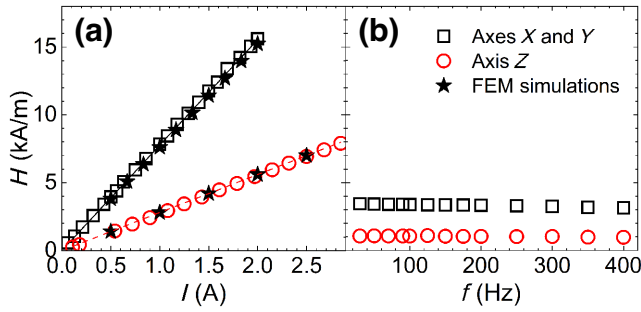
FIG. 4. (a) Field strength H versus dc current at the center of the device. Open symbols represent the experimental data, solid stars represent FEM simulations, and the lines are the best linear fits. (b) Field strength H versus ac frequency for a constant current amplitude of 0.5 A.

coming from the difficulty of aligning the teslameter probe with the corresponding axes.

The direction of the generated **H** was calibrated as well, demonstrating the absence of coupling between the X and Y yokes. The X and Y circuits were fed, respectively, with the currents

$$
\begin{aligned}
I_x &= \frac{H_0}{K_x} \cos(\alpha), \\
I_y &= \frac{H_0}{K_y} \sin(\alpha).
\end{aligned}
\tag{2}
$$

For a given value of the angle α, we measured the amplitude of **H** with a transverse teslameter probe, where we refer to the orientation of the transverse probe as β. We have repeated this measurement for different values of α with $H_0 = 9.6$ kA/m to build the plot in Fig. 6. Both the measurements and the FEM simulations fairly coincide with the curves representing the trigonometrical relationship given by $H(\beta) = H_0 \cos(\alpha - \beta)$ and, in all cases, the maximum value is close to the target value, so that the
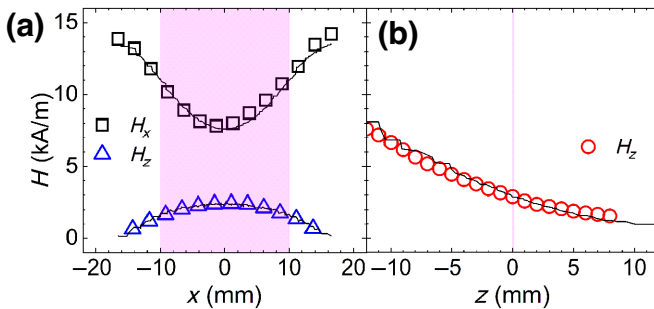

FIG. 5. (a) Plots of H_x and H_z along the X axis for $I_x = 1$ A and $I_z = 1$ A, respectively. (b) Plot of H_z along the Z axis for a current $I_z = 1$ A. Lines represent FEM simulation results. The shaded area represents the ROI.
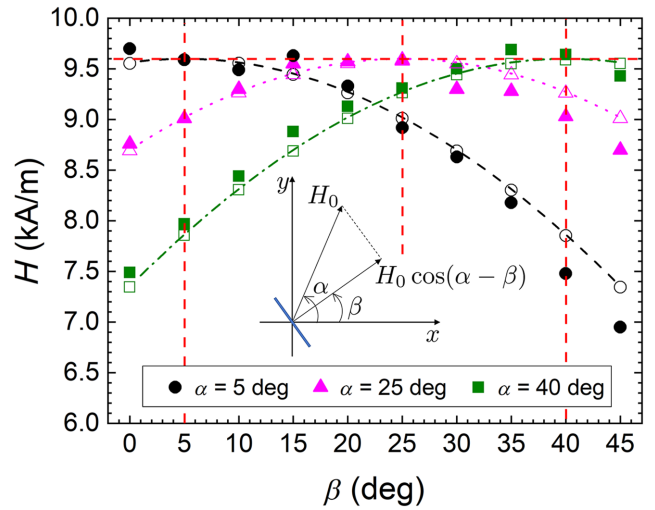

FIG. 6. Amplitude of **H** versus the orientation of the probe, where β is the angle between the probe and the X axis. The target amplitude was $H_0 = 9.6$ kA/m, indicated as a dashed horizontal line. The currents through the circuits were $I_x = H_0/K_x \cos(\alpha)$ and $I_y = H_0/K_y \sin(\alpha)$. The solid symbols are the experimental measurements, open symbols are FEM simulations and the curves represent the expected value $H(\beta) = H_0 \cos(\alpha - \beta)$. The vertical dashed lines represent $\beta = 5°$, $\beta = 25°$, and $\beta = 40°$, in other words, they represent, respectively, the angles at which the circles, the triangles, and the squares should reach the maximum value of 9.6 kA/m. The inset drawing represents the geometry of the test: the field **H** has magnitude H_0 and direction given by the angle α with respect to the X axis. The blue line represents a cross section of the transverse probe, which measures the component of **H** normal to its surface, i.e., the component of **H** forming an angle β with respect to the X axis.

amplitude of a rotating field generated by the instrument can be safely assumed to be constant.

The direction of **H** was also verified by means of aggregation experiments on 1-mm-diameter nickel beads. Details on this procedure are given in the Supplemental Material [32].

B. Aggregation of MR fluids under unsteady 3D fields

The characterization explained in the last subsection was performed with the generator in its *regular* configuration: the coils facing each other in the XY plane are in series and fed antisymmetrically, so that the field is as homogeneous as possible in the ROI. This is the adequate configuration for those experiments where, first, field gradients are not sought and, second, the device's capability to work at high frequencies needs to be exploited. Indeed, this is the proper configuration for applications such as the artificial swimmers mentioned in the introduction, where **H** is spatially homogeneous, but time dependent, for instance, rotating in a given plane. In these cases, the unsteady field imposes the rotation of individual swimmers or aggregates, which, due to their geometry and the hydrodynamical drag,

is converted in a linear motion. This *regular* configuration was used for the experiments reported in the remainder of this subsection, and we discuss a different approach in the following subsection, *Alternative operation modes*, where the motion of the magnetic particles is imposed by means of magnetophoretic forces created by nonhomogeneous fields.

As a proof of concept, in addition to the device characterization, we have used the *regular* configuration to apply spatially homogeneous nonsteady fields on a 1 vol.% concentration of carbonyl-iron (CI) particles dispersed in a 1:1 by volume water/glycerol solution. In order to test the 3D control of the device, we fed the circuits such that $\mathbf{H}(t)$ follows a particular case of the so-called *Pancake* curve, where each component is given by

$$
\begin{aligned}
H_x &= 7.77 \cos(2\pi f t), \\
H_y &= 7.77 \cos(2\pi f t - \pi/2), \\
H_z &= 2.8 \cos(4\pi f t - \pi/2).
\end{aligned}
\tag{3}
$$

This curve is represented in Fig. 7(a), where the amplitude of $\mathbf{H}$ is within 3% with respect to its mean value during a period, whereas its maximum vertical tilt is 19.8°. In order to ease the interpretation of this curve, it can be seen as a sine wave drawn on the surface of a cylinder having its axis along the Z direction. Note that the frequency of the alternating H_z is twice that of H_x and H_y. The upper panel in Fig. 8 shows representative snapshots of a particles aggregate for $f = 0.5$ Hz (see the Supplemental Material for the full video [32]). Since this frequency is low enough for the magnetic forces to dominate over the viscous forces, the aggregate follows the direction of the generated field, where the vertical tilt manifests as one of the tips leaving the focus of the image, and can be estimated from the apparent aggregate length. Therefore, this low-frequency case can be used as a benchmark for the actual direction of $\mathbf{H}$. As can be seen in Fig. 7(b), the horizontal orientation of the aggregate, θ, is rotating with angular frequency π rad/s, whereas the vertical tilt is alternating with angular frequency 2π rad/s, as expected.

The capability of the instrument to generate alternating and synchronized fields up to the kilohertz regime was tested by means of similar experiments, where the fractal capacitor banks and the feedback control loop are essential to ensure that both the amplitude of H_x, H_y, and H_z and their relative phases remain constant when increasing f. Representative snapshots for $f = 5$ Hz, $f = 10$ Hz, $f = 20$ Hz, $f = 100$ Hz, and $f = 1$ kHz are shown in the bottom panel of Fig. 8. When increasing f, the linearity of the aggregate vanishes and for $f > 5$ Hz the direction of the field and the orientation of the aggregate decouple. This can be clearly seen in Fig. 9, where, for $f > 5$ Hz, the orientation of the aggregate changes with time as
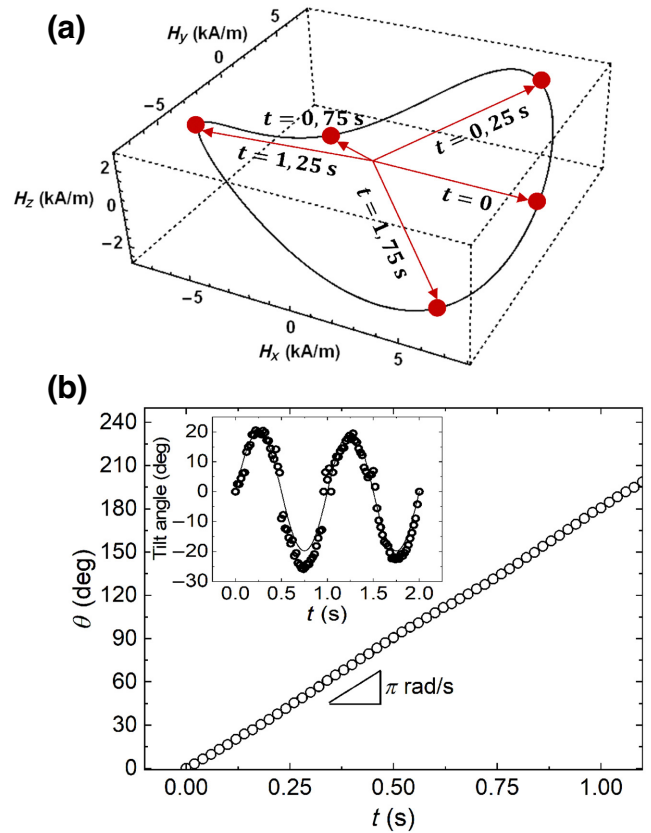

FIG. 7. (a) Pancake curve followed by the generated magnetic field, where the arrows represent $\mathbf{H}$ at the indicated times for the experiment with $f = 0.5$ Hz. The snapshots for these times are shown in the upper panel of Fig. 8. (b) Orientation of the aggregate for $f = 0.5$ Hz, with an indication of the slope for a uniform angular velocity of π rad/s. The inset represents the vertical tilt calculated from the aggregate's apparent length (symbols) and the expected value from Eq. (3) for $f = 0.5$ Hz (solid curve).

a combination of a uniform rotation and a periodical perturbation whose frequency increases with the frequency of the alternating field. Both the amplitude of the perturbation and the constant angular rate of rotation decrease with f. For $f = 100$ Hz and a maximum acquisition frequency of 500 fps, the aggregate's motion appears uniform, whereas the aggregate remains at rest for $f = 1$ kHz.

From a different experimental approach, this instrument has also been used to explore the aggregation in MR fluids under different field configurations. Fig. 10, reproduced from Ref. [36], shows the different structures that a 1 vol.% CI particle concentration in a 1:1 by volume water and glycerol solution manifests when is placed under (i) a precession field (dc along the Z axis plus rotating field in the XY plane, cases 1–6), and (ii) a biaxially perturbed field (dc along the Z axis plus alternating field along the X axis, cases 7 and 8) [36]. Different structures arise when the angle and frequency of the field change, even though
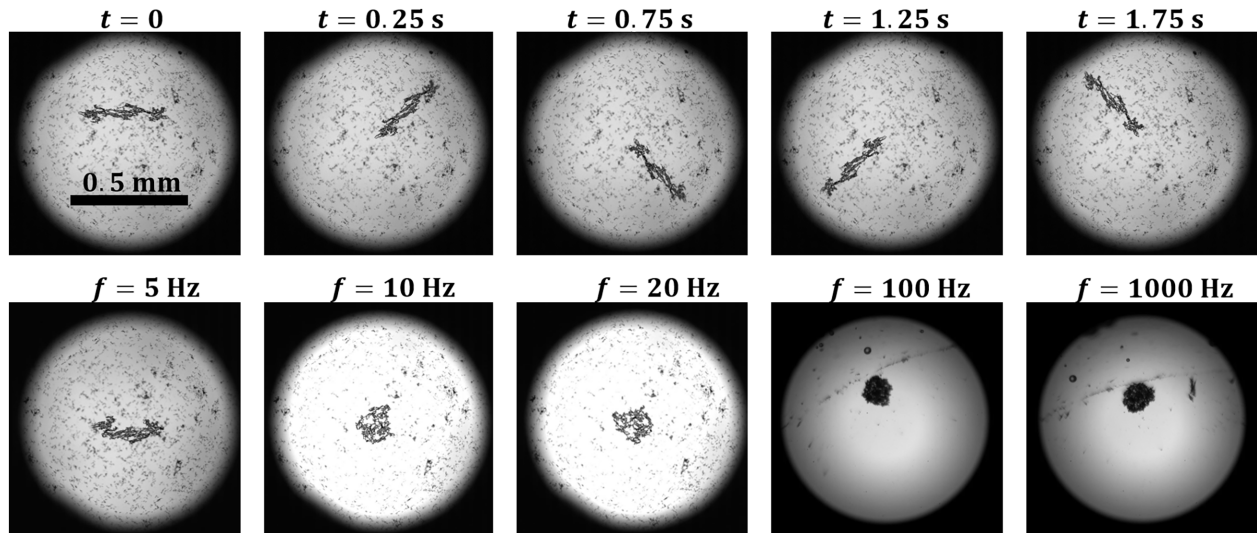
FIG. 8.   Snapshots of the aggregation experiment on a 1 vol.% concentration of carbonyl-iron particles dispersed in a 1:1 by volume water/glycerol solution under a pancake-curve-like magnetic field. The upper panel shows different time frames for the experiment with $f = 0.5$ Hz. The bottom panel shows images for increasing frequencies (see the Supplemental Material for the full videos [32]). We have analyzed these images to obtain (i) the orientation of the aggregate, θ, by tracking the orientation of the aggregate's principal axis, and (ii) the vertical tilt, calculated from the apparent length of the aggregate along its principal axis (this calculation was performed only for the lowest frequency, where the viscous forces are negligible with respect to the magnetic forces and the orientation of the aggregate can be directly compared with that of **H**). The results of this analysis is shown in the Figs. 7(b) and 9.

the field intensity was the same for all the experiments. The feedback control loop and the capacitor banks are fundamental to (i) ensure the same field intensity for all the configurations, (ii) avoid deviations from the prescribed direction for **H**, and (iii) allow for a controlled transition between different configurations, if needed (for instance, transitioning from a precessionlike field to a dc field by gradually removing the rotating field on the XY plane). For more details in these experiments, the reader is referred to Refs. [36,37].
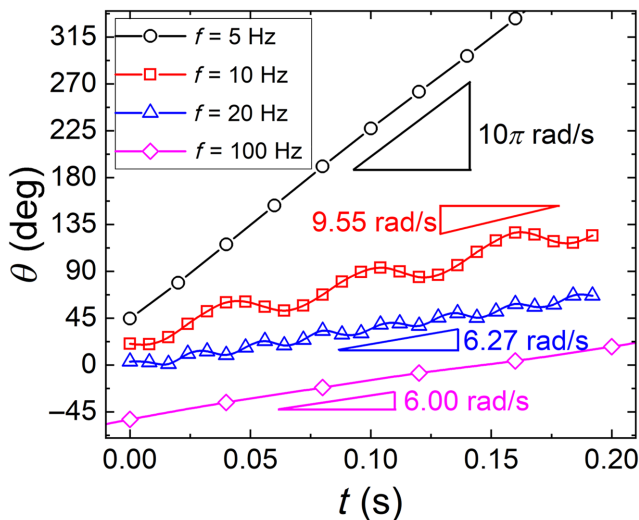
C. Alternative operation modes

In this subsection, we explain different field configurations that can be generated by modifying the wiring of the coils and the voltage signal driving the amplifiers. It is important to note that the operation modes that we depict in this subsection involve nonsinusoidal currents in the circuits, so that the benefit provided by the capacitor banks cannot be utilized. The main feature exploited in this subsection is the capability of generating arbitrary voltage signals from the LabVIEW code developed for this instrument. We find it illustrative to explain these alternative modes, although they can be applied only for low frequencies.

FIG. 9.   Direction of the aggregate's principal axis versus time for different frequencies. For $f = 5$ Hz, the slope indication, 10π rad/s, represents the frequency of the imposed field. For $f > 5$ Hz, the slope indication represents the constant angular rate of rotation calculated from the linear fit of the experimental data.

1. Pulses generation

For the frequencies of interest in this work, the generated magnetic field H is proportional to the commanded current I. Hence, to generate a pulse in H we need to create a pulse in I. However, since any inductance opposes to changes in I, a perfect square waveform in I (or H) is not feasible. The deviation of the actual shape of the I waveform
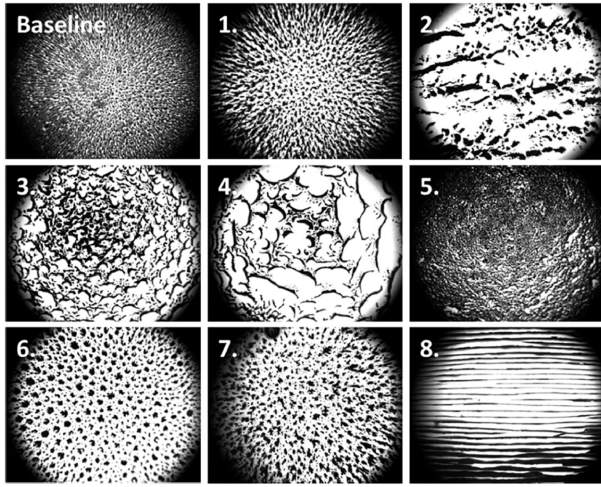
FIG. 10. CI MR fluid under different field configurations. Baseline: dc field along the Z axis. 1: Precession field with angle of 15° and $f = 10$ Hz. 2–5: Precession field with angle of 75° and frequency of 0.01, 1, 10, and 100 Hz, respectively. 6: Precession field with angle of 15° and $f = 1$ Hz. 7 and 8: dc field along the Z direction plus a periodical perturbation along the X direction with angle of 60° and frequency of 0.1 and 10 Hz, respectively. Reproduced with permission from M. Terkel and J. de Vicente, Smart Mater. Struct. 30, 014005 (2020). Copyright 2020, IOP Publishing.

FIG. 11. (a) Voltage at the output terminals of the amplifier feeding the X circuit, where the solid line is the measurement when a regular pulse with amplitude $V_p = 10$ V and frequency $f_p = 10$ Hz is generated, and the dashed curve represents the measurement when the signal driving the amplifier is generated by means of LabVIEW using Eq. (5). (b) Current through the circuit when it is fed with the regular and modified pulses shown in (a). As expected, the transient time is reduced for the modified pulse, so that the magnetic field at the ROI follows more closely the desired square wave shape.

from a square waveform increases with the frequency and amplitude of the pulse. In this subsection, we discuss how to optimize the field pulse generation by taking advantage of the custom-made LabVIEW code driving the amplifiers. The connection and short-circuit currents in an R–L circuit are given by

$$
\begin{aligned}
i(t) &= \frac{V_p}{R}\left(1 - e^{-\frac{R}{L}t}\right), \\
i(t) &= \frac{V_p}{R}e^{-\frac{R}{L}t},
\end{aligned}
\tag{4}
$$

respectively, where V_p is the applied voltage. Considering the impedances of the circuits, the exponential time constant of our device is $L/R \sim 10$ ms. Therefore, when the frequency of the applied pulse is above ~ 10 Hz, the current significantly deviates from a square signal. The current can be easily made more pulselike as long as $V_p < V_m$, where V_m is the maximum output voltage of the amplifier. Indeed, the time necessary to reach the stationary current, V_p/R, can be decreased by applying V_m at the rising edge of the pulse for the proper interval of time. The same strategy can be replicated in the falling edge of the pulse, applying a voltage $-V_m$ in this turn. The capability of LabVIEW to generate arbitrary analog signals has been utilized to drive the amplifiers with a periodical signal
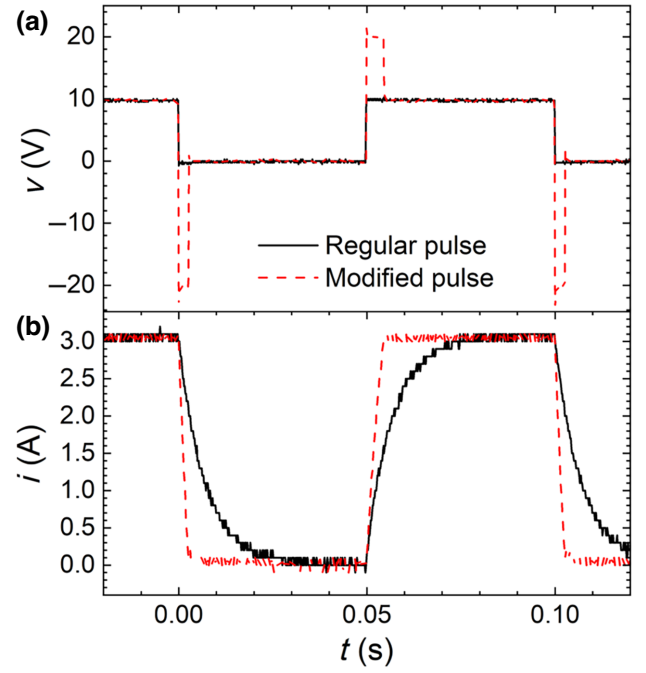
given by

$$
v(t) =
\begin{cases}
V_m, & t \le -\frac{L}{R}\log\left(1 - \frac{V_p}{V_m}\right), \\
V_p, & -\frac{L}{R}\log\left(1 - \frac{V_p}{V_m}\right) < t \le \frac{1}{2f_p}, \\
-V_m, & \frac{1}{2f_p} < t \le \frac{1}{2f_p} - \frac{L}{R}\log\left(1 - \frac{V_p}{V_m + V_p}\right), \\
0, & \frac{1}{2f_p} - \frac{L}{R}\log\left(1 - \frac{V_p}{V_m + V_p}\right) < t.
\end{cases}
\tag{5}
$$

The result of applying this strategy to generate a 10-Hz pulse and its comparison with the performance of a simple square voltage waveform is shown in Fig. 11, where the improvement in the current signal is clear.

2. Magnetic tweezers configuration

In all the tests discussed so far the two coils corresponding to each X and Y axes are connected in series and the current flows in the same direction. Hence, by symmetry, $\partial H_{x,y}/\partial x, y = 0$ at the center of the device. This configuration is ideal to generate homogeneous magnetic

fields avoiding magnetophoretic forces. However, nonhomogeneous magnetic fields can also be easily generated and, accordingly, the device used as a two-dimensional magnetic tweezers apparatus. Constraining our discussion to the X axis, such a nonhomogeneous magnetic field can be generated if the two coils on the X axis are fed independently, with currents

$$\begin{aligned} I_{x1} &= \delta I + I_0, \\ I_{x2} &= \delta I - I_0. \end{aligned} \tag{6}$$

Note that under these conditions, both the magnetic field and the gradient have nonzero values at the center of the ROI. In particular,

$$\begin{aligned} H_x &= K_x\,\delta I, \\ \frac{\partial H_x}{\partial x} &\propto I_0. \end{aligned} \tag{7}$$

In an attempt to test this operation mode in a dynamic way, we generated an oscillatory field gradient by means of feeding the two X coils with the currents

$$\begin{aligned} I_{x1} &= \delta I + I_0 \cos(\omega t), \\ I_{x2} &= \delta I - I_0 \cos(\omega t). \end{aligned} \tag{8}$$

In this configuration, the constant current δI is used to fix the magnitude of H and, therefore, the magnetization of the magnetic probe, whereas the oscillating current I_0 is used to generate a controlled field gradient. Given the magnitude of the magnetic fields generated by this instrument, the probe magnetization is expected to be proportional to H, which makes the magnetic force on the probe proportional to $\nabla(H^2)$. However, if the maximum displacement of the probe from the center of the ROI, Δx, is small enough to satisfy $H_x \gg \Delta x\, \partial H_x/\partial x$, the magnetization of the probe can be safely considered constant. Under these circumstances, the magnetic force applied on the probe is closely proportional to the product $I_0 \delta I$.

We tested this configuration by applying the currents $I_0 = 0.27$ A and $\delta I = 0.36$ A, which yield values of the field and its gradient of $H_x = 2.8$ kA/m and $\partial H_x/\partial x = 0.32$ kA/(m mm). We explored two frequencies, 0.1 and 0.5 Hz, and we used a 47 μm in radius "pickering" droplet of decane coated by CI particles immersed in water as a field probe [38]. The motion of the droplet was tracked by means of a videomicroscopy inspection system and the reconstruction of its coordinates yields a maximum displacement of $\Delta x \simeq 0.5$ mm. Therefore, the product $\Delta x\, \partial H_x/\partial x \simeq 0.16$ kA/m, so that the magnetization of the probe varies in less than $\pm 6\%$ during its oscillatory motion. Figure 12 shows the displacement of the droplet versus time, with a good agreement between the experimental data and the sine function represented in the curve. As discussed previously, under these circumstances, the actual
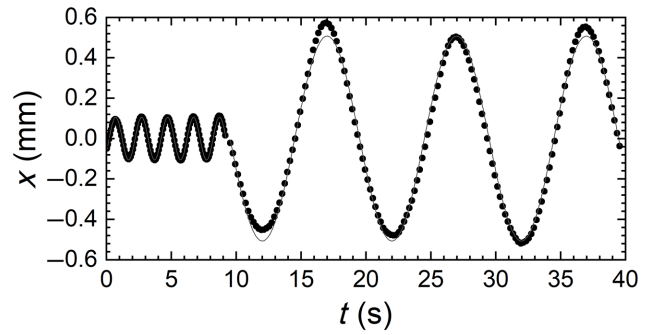

FIG. 12. Displacement of the "pickering" droplet versus time. Symbols represent experimental data and the solid curves are the best fit to a sine function. Two frequencies were explored, 0.5 Hz and 0.1 Hz. In both cases, an homogeneous field generated by $\delta I = 0.36$ A is superimposed with an oscillatory field gradient generated by $I_0 = 0.27$ A.

force on the magnetic probe is proportional to the applied current, demonstrating that the generator is also suitable for being used as a magnetic tweezers apparatus.

A simple hydrodynamical model for the droplet motion (see Supplemental Material for details [32]) yields a force to displacement ratio given by

$$\frac{F_{\mathrm m}}{A} = \sqrt{(\omega 6\pi R\eta)^2 + (m\omega^2)^2}, \tag{9}$$

where $F_{\mathrm m}$ is the amplitude of the oscillating magnetic force imposed on the CI particles coating the droplet, A is the amplitude of the oscillatory motion followed by the droplet, R is the droplet radius, η is the viscosity of the surrounding fluid (water), and m is the droplet mass. For frequencies as low as 0.5 Hz, $6\pi R\eta \gg m\omega$, so that the inertial term does not play a significant role in the droplet dynamics and the amplitude ratio satisfies $F_{\mathrm m}/A \propto \omega$. The amplitude of the best fits to sine functions represented in Fig. 12 are 105 μm and 507 μm for $f = 0.5$ Hz and $f = 0.1$ Hz, respectively. This result is consistent with the inertial term being negligible because the ratio of the amplitudes, 105/507, is roughly equivalent to the ratio of the frequencies, 0.1/0.5. The order of magnitude of the magnetic force applied on the droplet can be estimated from this simple hydrodynamical model as well. The only unknown in Eq. (9) is $F_{\mathrm m}$, which, from the measured amplitude motion, results in ~ 0.28 nN. Assuming a volume magnetic susceptibility of $\chi \sim 1.95$ [36] for the CI particles and the magnetic field intensity and gradient reported previously, the applied force per unit volume of magnetic material is ~ 2200 nN/μL. Thus, the magnetic volume results in $\sim 0.28/2200 \simeq 1.3 \times 10^{-4}$ μL, which is, bearing in mind that CI particles have a radius of 2 μm, in reasonable agreement with the volume of a spherical shell with outer and inner radii of 47 μm and 43 μm, respectively (1.02×10^{-4} μL).

The use of this instrument as a stress-controlled rheometer to measure the mechanical properties of the surrounding fluid would require a finer calibration of the magnetic force, but the simple hydrodynamical model depicted in this Subsection and the good agreement between (i) the expected and measured dependence of F_m/A on the frequency and (ii) the expected and calculated magnetic volume, indicates that the actual field intensity and field gradient generated by the device are very close to those measured and calculated through the FEM simulations (Figs. 4 and 5). Moreover, an order of magnitude estimation of the upper limit in the magnetic force can be extrapolated from the previous analysis. Let us assume that the maximum currents safely attainable by the generator are $I_0 = \delta I \sim 2\,\text{A}$, and the magnetic probes are CI particles with $\chi = 1.95$, as in the "pickering" droplet experiment. The magnetic force per volume must be, in this case, $2^2/(0.27 \times 0.36) \simeq 41$ times larger than that imposed on the droplet ($F_m/V \sim 9 \times 10^4\,\text{nN}/\mu\text{L}$). Therefore, the maximum force that this instrument can exert on a single CI particle with radius $2\,\mu\text{m}$ is, approximately, $F_{max} \sim \frac{4}{3}\pi(2 \times 10^{-6})^3 F_m/V \sim 3\,\text{pN}$.

IV. CONCLUSIONS

A triaxial magnetic field generator has been designed, constructed and calibrated. It employs three R–L–C circuits to induce each field component. In order to optimize the ac operation mode, the capacitive element of each circuit consists in a fractal capacitor bank. This setup provides a quasi-continuous distribution of resonant frequencies from $\sim 40\,\text{Hz}$ to $\sim 4\,\text{kHz}$. The three circuits forming the device work independently, but they are synchronized through a feedback control loop and a LabVIEW software. The fine control on the initial phase and amplitude of the intensity currents allows for the generation of a magnetic field following any Lissajous figure in three dimensions.

The H/I ratio for each circuit has been measured in dc and ac configurations, and the direction of the generated field has been crosschecked by means of both, direct measurements with a teslameter, and videomicroscopy of particle aggregates oriented with the field. Two alternative operation modes have been described as well: we demonstrate the possibility to generate H pulses, by using the maximum power of the amplifiers to decrease the transient time, and magnetophoretic forces, by the independent feeding of the coils along the same axes. The experiments reported here allow us to estimate that, with this instrument, the maximum magnetophoretic force on micrometer-sized particles is of the order of 1 pN, whereas homogeneous alternating fields of up to 10 kA/m in amplitude can be generated with frequencies as high as 1 kHz.

[1] R. Dreyfus, J. Baudry, M. L. Roper, M. Fermigier, H. A. Stone, and J. Bibette, Microscopic artificial swimmers, Nature **437**, 862 (2005).

[2] L. Zhang, J. J. Abbott, L. Dong, B. E. Kratochvil, D. Bell, and B. J. Nelson, Artificial bacterial flagella: Fabrication and magnetic control, Appl. Phys. Lett. **94**, 064107 (2009).

[3] J. Yu, B. Wang, X. Du, Q. Wang, and L. Zhang, Ultra-extensible ribbon-like magnetic microswarm, Nat. Commun. **9**, 1 (2018).

[4] H. Xie, M. Sun, X. Fan, Z. Lin, W. Chen, L. Wang, L. Dong, and Q. He, Reconfigurable magnetic microrobot swarm: Multimode transformation, locomotion, and manipulation, Sci. Robot. **4**, eaav8006 (2019).

[5] D. Ahmed, T. Baasch, N. Blondel, N. Läubli, J. Dual, and B. J. Nelson, Neutrophil-inspired propulsion in a combined acoustic and magnetic field, Nat. Commun. **8**, 1 (2017).

[6] D. Ahmed, A. Sukhov, D. Hauri, D. Rodrigue, G. Maranta, J. Harting, and B. J. Nelson, Bioinspired acousto-magnetic microswarm robots with upstream motility, Nat. Mach. Intell. **3**, 116 (2021).

[7] T. Tasci, P. Herson, K. Neeves, and D. Marr, Surface-enabled propulsion and control of colloidal microwheels, Nat. Commun. **7**, 1 (2016).

[8] V. Kantsler, J. Dunkel, M. Blayney, and R. E. Goldstein, Rheotaxis facilitates upstream navigation of mammalian sperm cells, eLife **3**, e02403 (2014).

[9] K. Miki and D. E. Clapham, Rheotaxis guides mammalian sperm, Curr. Biol. **23**, 443 (2013).

[10] E. Lauga, W. R. DiLuzio, G. M. Whitesides, and H. A. Stone, Swimming in circles: motion of bacteria near solid boundaries, Biophys. J. **90**, 400 (2006).

[11] T. Kaya and H. Koser, Direct upstream motility in Escherichia coli, Biophys. J. **102**, 1514 (2012).

[12] W. M. Durham and R. Stocker, Thin phytoplankton layers: characteristics, mechanisms, and consequences, Annu. Rev. Mar. Sci. **4**, 177 (2012).

[13] D. Walker, B. T. Käsdorf, H.-H. Jeong, O. Lieleg, and P. Fischer, Enzymatically active biomimetic micropropellers for the penetration of mucin gels, Sci. Adv. **1**, e1500501 (2015).

[14] A. Servant, F. Qiu, M. Mazza, K. Kostarelos, and B. J. Nelson, Controlled in vivo swimming of a swarm of bacteria-like microrobotic flagella, Adv. Mater. **27**, 2981 (2015).

[15] O. Felfoul, M. Mohammadi, S. Taherkhani, D. De Lanauze, Y. Zhong Xu, D. Loghin, S. Essa, S. Jancik, D. Houle, M. Lafleur, L. Gaboury, M. Tabrizian, N. Kaou, M. Atkin, T. Vuong, G. Batist, N. Beauchemin, D. Radzioch,

and S. Martel, Magneto-aerotactic bacteria deliver drug-containing nanoliposomes to tumour hypoxic regions, Nat. Nanotechnol. **11**, 941 (2016).

[16] R. Blakemore, Magnetotactic bacteria, Science **190**, 377 (1975).

[17] J. Lyklema, *Fundamentals of Interface and Colloid Science: Particulate Colloids* (Elsevier Ltd, London, 2005).

[18] J. de Vicente, D. J. Klingenberg, and R. Hidalgo-Alvarez, Magnetorheological fluids: a review, Soft Matter **7**, 3701 (2011).

[19] J. E. Martin and A. Snezhko, Driving self assembly and emergent dynamics in colloidal suspensions by time dependent magnetic fields, Rep. Prog. Phys. **76**, 126601 (2013).

[20] P. Skalski and K. Kalita, Role of magnetorheological fluids and elastomers in today's world, Acta Mech. et Autom **11**, 267 (2017).

[21] J. W. Swan, J. L. Bauer, Y. Liu, and E. M. Furst, Directed colloidal self-assembly in toggled magnetic fields, Soft Matter **10**, 1102 (2014).

[22] J. W. Swan, P. A. Vasquez, P. A. Whitson, E. M. Fincke, K. Wakata, S. H. Magnus, F. De Winne, M. R. Barratt, J. H. Agui, R. D. Green, N. R. Hall, D. Y. Bohman, C. T. Bunnell, A. P. Gast, and E. M. Furst, Multi-scale kinetics of a field-directed colloidal phase transition, Proc. Natl. Acad. Sci. **109**, 16023 (2012).

[23] J. E. Martin, E. Venturini, J. Odinek, and R. A. Anderson, Anisotropic magnetism in field-structured composites, Phys. Rev. E **61**, 2818 (2000).

[24] J. R. Morillas and J. de Vicente, Magnetorheology: a review, Soft Matter **16**, 9614 (2020).

[25] S. Melle, O. G. Calderón, G. G. Fuller, and M. A. Rubio, Polarizable particle aggregation under rotating magnetic fields using scattering dichroism, J. Colloid Interface Sci. **247**, 200 (2002).

[26] J. Černák and G. Helgesen, Aggregation of magnetic holes in a rotating magnetic field, Phys. Rev. E **78**, 061401 (2008).

[27] R. Moctezuma, F. Donado, and J. Arauz-Lara, Lateral aggregation induced by magnetic perturbations in a magnetorheological fluid based on non-Brownian particles, Phys. Rev. E **88**, 032305 (2013).

[28] F. Donado, J. Sausedo-Solorio, and R. Moctezuma, Dynamical and structural properties of a granular model for a magnetorheological fluid, Phys. Rev. E **95**, 022601 (2017).

[29] F. Martinez-Pedrero and P. Tierno, Magnetic propulsion of self-assembled colloidal carpets: efficient cargo transport via a conveyor-belt effect, Phys. Rev. Appl. **3**, 051003 (2015).

[30] K. J. Solis and J. E. Martin, Stimulation of vigorous rotational flows and novel flow patterns using triaxial magnetic fields, Soft Matter **8**, 11989 (2012).

[31] J. E. Martin, On the origin of vorticity in magnetic particle suspensions subjected to triaxial fields, Soft Matter **12**, 5636 (2016).

[32] See Supplemental Material at http://link.aps.org/supplemental/10.1103/PhysRevApplied.20.044063 for details of the magnetic field generator and capacitor banks (their calibration, feedback control loop, and modeling using FEM simulations), a model for the motion of the pickering droplet in the magnetic tweezers configuration as well as 10 videos showing the aggregation experiment under pancake-curve-like magnetic fields of different frequencies.

[33] D. Siemaszko, C. Rod, and A. C. Rufer, Single-phase resonant *LC* circuit using a bank of self-switched capacitors, IEEE Trans. Ind. Electron. **58**, 4175 (2011).

[34] S. Li, K. Xiangli, Y. Zheng, and K. M. Smedley, Analysis and design of the ladder resonant switched-capacitor converters for regulated output voltage applications, IEEE Trans. Ind. Electron. **64**, 7769 (2017).

[35] J. E. Martin, A resonant biaxial Helmholtz coil employing a fractal capacitor bank, Rev. Sci. Instrum. **84**, 094704 (2013).

[36] M. Terkel and J. de Vicente, Magnetorheology of exotic magnetic mesostructures generated under triaxial unsteady magnetic fields, Smart Mater. Struct. **30**, 014005 (2020).

[37] M. Terkel, J. Tajuelo, and J. de Vicente, Enhancing magnetorheology with precession magnetic fields, J. Rheol. **66**, 67 (2022).

[38] S. Melle, M. Lask, and G. G. Fuller, Pickering emulsions with controllable stability, Langmuir **21**, 2158 (2005).